Finite-temperature study of the Hubbard model via enhanced exponential tensor renormalization group

Changkai Zhang (张昌凯) and Jan von Delft
Arnold Sommerfeld Center for Theoretical Physics, Center for NanoScience, and Munich Center for Quantum Science and Technology, Ludwig-Maximilians-Universität München, 80333 Munich, Germany

(Received 15 December 2025; revised 6 July 2026; accepted 13 July 2026; published 18 August 2026)

The two-dimensional (2D) Hubbard model has long attracted interest for its rich phase diagram and its relevance to high-T_c superconductivity. However, reliable finite-temperature studies remain challenging due to the exponential complexity of many-body interactions. Here, we introduce an enhanced 1s$^+$ exponential tensor renormalization group algorithm that enables efficient finite-temperature simulations of the 2D Hubbard model. By exploring an expanded space, our approach achieves two-site update accuracy at the computational cost of a one-site update, and delivers up to 50% acceleration for Hubbard-like systems, which enables simulations down to $T \approx 0.004t$. This advance permits a direct investigation of superconducting order over a wide temperature range and facilitates a comparison with zero-temperature infinite projected entangled pair state simulations. Finally, we compile a comprehensive dataset of snapshots spanning the relevant region of the phase diagram, providing a valuable reference for artificial-intelligence-driven analyses of the Hubbard model and a comparison with cold-atom experiments.

DOI: 10.1103/7m9y-v22h

I. INTRODUCTION

High-T_c superconductivity in cuprate materials has attracted immense research interest ever since its discovery [1–5]. The two-dimensional (2D) Hubbard model [6,7] on a square lattice is widely believed to capture the essential physics of these systems, particularly the effects of strong electron correlations. In recent years, extensive research has been carried out to explore the ground-state (zero-temperature) properties of the Hubbard model [8–47] or its simplified counterpart, t-J model [48–65]. In particular, long-range or quasi-long-range pairing orders, indicative of robust superconductivity, have been observed in the presence of a positive next-nearest-neighbor hopping amplitude t' [37,44,47,57–59,63–65]. This naturally raises the question of how much such superconducting behavior extends to higher temperatures.

However, finite-temperature studies of the Hubbard model remain challenging due to the limitations of traditional numerical techniques. For example, the finite-temperature Lanczos method is constrained to small system sizes [66–68], while quantum Monte Carlo (QMC) is plagued by the notorious sign problem at finite doping [69,70]. In this context, thermal tensor network algorithms have emerged as promising alternatives. [71–89]. In particular, the exponential tensor renormalization group (XTRG) [78] method excels in performing exponentially rapid cooling of the system, albeit at the cost of relatively high computational complexity.

In this work, we apply the controlled bond expansion (CBE) technique [90–92] originally designed for matrix product state (MPS) methods such as density matrix renormalization group (DMRG) [91] and time-dependent variational principle [92] to products of matrix product operators (MPOs), thereby introducing an enhanced 1s$^+$ XTRG algorithm. By exploring an enlarged variational space, our scheme attains two-site update accuracy at a much lower computational complexity, delivering up to a 50% acceleration for Hubbard-like systems. This improvement enables cooling down to $T/t = 1/256$ (approximately 20 K for $t = 0.3 \sim 0.5$ eV) and facilitates quantitative comparison with zero-temperature infinite projected entangled pair state (iPEPS) results [47]. Pairing correlations are found to be enhanced at positive next-nearest-neighbor (NNN) hopping ratio t'/t, and the pseudogap behavior, together with a possible Nagaoka polaron, is identified through the temperature dependence of the spin susceptibility. Finally, we generate and validate a comprehensive dataset of snapshots spanning the underdoped, intermediate-doped, and overdoped regimes across high, medium, and low temperatures. This dataset offers valuable resources for future artificial-intelligence (AI)-driven analyses [93,94] of the Hubbard model and for comparison or calibration of cold-atom experiments [83,94–108].

II. MODEL AND METHOD

In this paper, we consider the 2D t-t' Hubbard model on an 8×8 square lattice with periodic boundary conditions (PBC) on the y direction and open boundary conditions (OBC) on the x direction unless stated otherwise. The Hamiltonian is

defined as

$$\mathcal{H} = -\sum_{i,j,\sigma} t_{ij}[c^\dagger_{i\sigma} c_{j\sigma} + \text{H.c.}] + U\sum_i n_{i\uparrow} n_{i\downarrow}. \tag{1}$$

Here, $t_{ij} = t$ or t' for nearest-neighbor (NN) or NNN hopping amplitude, respectively, and zero otherwise; U measures the on-site Coulomb repulsion. Throughout this paper, we use $U/t = 10$, as established to be realistic for cuprate materials [109,110], and set $t = 1$ for convenience.

A comparison of band structure between cuprate superconductors and the Hubbard model suggests a positive t'/t ratio for electron-doped cuprates and a negative t'/t for hole-doped cuprates [109,110]. However, we note that this identification leads to inconsistencies between model predictions and experimental observations for crucial order parameters, as reported previously [47,88,111] and further corroborated in the present work (see Sec. VI on pair-pair correlations).

The XTRG algorithm [78] provides an efficient framework for constructing the thermal density matrix $\rho = \exp(-\beta\mathcal{H})$ of a quantum many-body system in the form of a MPO, where $\beta = 1/T$ is the inverse temperature. Specifically, an initial density matrix $\rho(\beta_0)$ is prepared at a high temperature (small $\beta_0 = 2^{-n_0}$) via the series expansion

$$\rho(\beta_0) = \mathbb{1} - \beta_0\mathcal{H} + \frac{1}{2!}\beta_0^2\mathcal{H}^2 + \cdots. \tag{2}$$

The density matrix at half the temperature, or equivalently, at inverse temperature 2β, is then obtained by squaring the density matrix at β:

$$\rho(2\beta) = \exp\{-2\beta\mathcal{H}\} = \rho(\beta)\rho(\beta). \tag{3}$$

After n iterations, one reaches an inverse temperature of $2^n\beta_0$, realizing an exponentially fast cooling of the system. The principal computational bottleneck in XTRG thus lies in the efficient MPO-MPO product.

Analogous to the DMRG, XTRG supports both one-site and two-site update schemes for MPO-MPO products. The one-site update is computationally cheaper but limited by a restricted variational space. The two-site update overcomes this limitation by exploring a larger variational manifold, at the cost of much higher computational complexity.

The controlled bond expansion (CBE) technique [90–92] offers a balanced compromise: by modestly enlarging the variational space, CBE achieves near two-site update accuracy while maintaining a cost closer to that of the one-site update. In the following section, we demonstrate how the CBE technique can be adapted to the MPO-MPO product, leading to a $1s^+$ scheme that significantly accelerates the XTRG algorithm.

Our simulations employ the state-of-the-art QSpace tensor library [112–115], which preserves the $U(1)_{\text{charge}} \times SU(2)_{\text{spin}}$ symmetry in the MPO representation of the thermal density matrix. This allows us to retain up to $D^* = 1500$ multiplets (approximately $D \simeq 4000$ individual states), ensuring sufficient convergence of the XTRG algorithm.

III. $1s^+$ MPO-MPO PRODUCT

The MPO-MPO product constitutes a fundamental, and often the most computationally demanding, kernel in the XTRG algorithm. Both computing powers of $\mathcal{H}$ in the series expansion of $\rho(\beta_0)$ and performing the cooling step entail repeated MPO-MPO multiplications. A naive contraction of two MPOs with bond dimension D yields an MPO of bond dimension D^2; compressing it back to D via a straightforward singular value decomposition (SVD) incurs a cost of $O(D^6)$. This overhead naturally motivates the development of variational compression schemes.

In the variational approach, one posits an ansatz for the target MPO and optimizes its proximity to the exact product. Concretely, given MPOs A and B with product $A \circ B$, we seek an MPO C that minimizes the squared Frobenius norm of the discrepancy [78]

$$\|C - A \circ B\|_F^2 = C^\dagger C - C^\dagger(A \circ B) + \text{H.c.} + \text{const.}, \tag{4}$$

where $\circ$ denotes the MPO-MPO product. The optimization proceeds by sweeping along the chain and alternately updating one tensor at a time (one-site update, or 1s) or two adjacent tensors (two-site update, or 2s), while keeping all others fixed. The one-site update requires solving the linear system

$$\frac{\partial C^\dagger C}{\partial C_i^*} = \frac{\partial C^\dagger(A \circ B)}{\partial C_i^*} \tag{5}$$

iteratively for $i = 1, 2, \ldots, L$, where L is the length of the MPO chain. For canonicalized MPOs, the left-hand side collapses to the tensor C_i to be updated (denoted as 1s below). Diagrammatically, the one-site update reads [78]

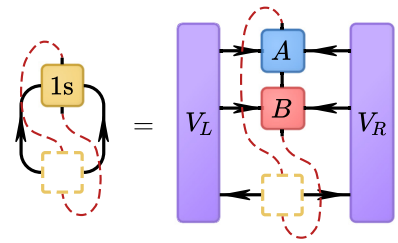

(6)

To circumvent the clutter introduced by twisty lines for physical indices, we streamline the notation by rearranging the physical indices as follows:

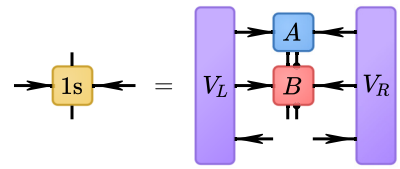

(7)

where the environment tensors V_L and V_R are precomputed and held fixed during the one-site update. The semicircles at the contact points between the physical index and tensor B indicate that the physical index passes through without contraction.

A prevalent flaw of the one-site update is its inability to enlarge the variational space in the presence of symmetry constraints. As implied by Eq. (7), the updated tensor remains confined to the symmetry sector of the original tensor. This constraint can be alleviated by the two-site update, which simultaneously optimizes two neighboring tensors, i.e.,

$$\frac{\partial C^\dagger C}{\partial (C_i C_{i+1})^*} = \frac{\partial C^\dagger(A \circ B)}{\partial (C_i C_{i+1})^*}. \tag{8}$$

Diagrammatically, the two-site update reads [78]

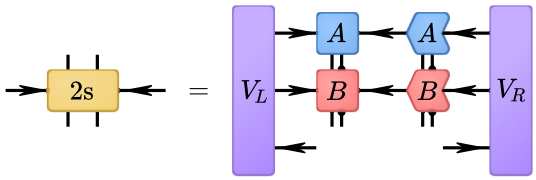

(9)

The meaning of the polygon-shaped tensor will be clarified later. The optimized two-site tensor is then decomposed via an SVD to produce the updated MPO tensors, i.e.,

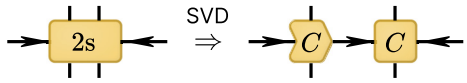

(10)

Note that a full SVD in Eq. (10) generates in total Dd^2 components, where d is the physical Hilbert-space dimension, whereas only the leading D components are ultimately retained. Consequently, most components are computed only to be discarded, squandering computational resources. Our $1s^+$ scheme mitigates this inefficiency by injecting only a small fraction of additional components, thereby enlarging the accessible variational space without incurring the full cost of a two-site update.

In the spirit of Ref. [90], a full MPO tensor admits a decomposition into a discarded-space component and a kept-space component

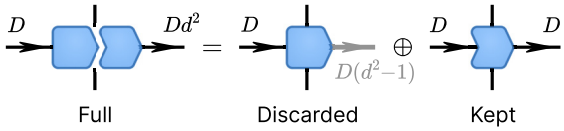

(11)

In our notation, tensors are depicted as (composite) polygons. The discarded component is denoted by a pentagon with a wedge, and the kept component by a polygon with both a wedge and a notch. Gray lines indicate components from the discarded space. The protruding face indicates the direction toward the orthogonality center of the MPO, or equivalently, the opposite direction to the normalization. In the example above, the MPO tensors are left normalized, placing the orthogonality center to the right of the tensor. Directions of the arrows encode the flow of quantum numbers, following the convention of Ref. [114].

Similar to the CBE technique [91], the discrepancy between the variational spaces accessible to the one-site and two-site updates can be identified by the following construction:

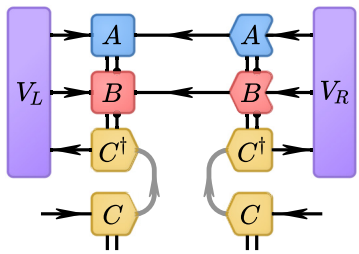

(12)

The two-site discarded-space tensor spans the variational sector accessible to the two-site update but excluded from the one-site manifold. An exact construction of this tensor would incur a computational cost $O(D^4d^4)$ comparable to a full two-site update. The dominant cost resides in the contraction of the left and right part of the above two-site tensor. Therefore, for practical purposes, we instead distill its principal components by performing the following SVD:

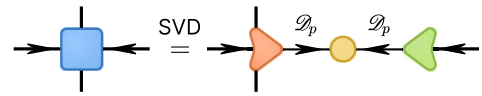

(13)

and retain only the leading $\mathscr{D}_p$ components. Here, $\mathscr{D}_p$ serves as a hyperparameter that controls the fidelity of the two-site discarded-space approximation. In our simulations, we choose $\mathscr{D}_p = \text{round}(\sqrt{D})$ to balance accuracy against computational overhead. With this construction, the green tensor acts as a projector that compresses the bond dimension further down to $\mathscr{D}_p$. The principal components of the two-site discarded-space tensor are then extracted by inserting these projectors as

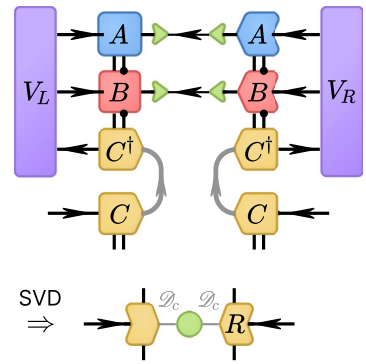

(14)

We emphasize that this procedure yields only an approximation to the principal components. In practice, exact identification of the principal components are unnecessary: the goal is to efficiently isolate the principal subspace that complements the one-site update, after which subsequent optimization sweeps would converge to the desired solution.

We now outline the ensuing steps for a left-to-right optimization sweep; the right-to-left sweep proceeds analogously. The two-site discarded-space tensor is decomposed and truncated to $\mathscr{D}_c$ via an SVD [see Eq. (14)], yielding the isometry R tailored for the left-to-right sweep. The tensor R thus serves as the supplement to the MPO tensor on the right. In our computations, we set $\mathscr{D}_c = \text{round}(\sqrt{D})$. Next, the left supplement tensor, L, is obtained by

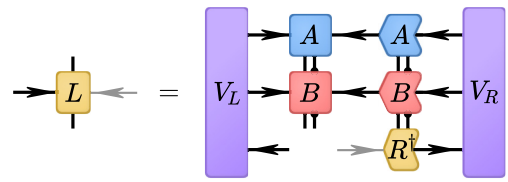

(15)

Tensors L and R thus offers the additional components that augment the variational space. Equipped with these ingredients, we assemble the expanded MPO tensors L^+ and R^+ as

follows:

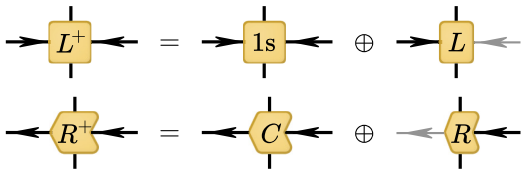

(16)

Contracting L^+ and R^+ produces a tensor analogous to the two-site object in Eq. (10), albeit with substantially fewer auxiliary components. The updated MPO tensors are then obtained by applying an SVD and truncating to the leading D components

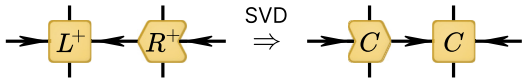

(17)

The canonical two-site update exhibits a computational complexity $O(D^4d^4)$, where d denotes the physical dimension of the MPO tensors; this scaling is dominated by constructing the updated two-site tensors. By contrast, the $1s^+$ scheme reduces the complexity to the one-site level, i.e., $O(D^4d^2)$, thereby shifting the computational bottleneck to constructing the environmental tensors V_L and V_R. Consequently, the overall complexity of the $1s^+$ scheme is $O(D^4d^2 + D^4d^3)$. For Hubbard-like systems, the physical dimension $d = 4$, rendering a maximum $4\times$ speedup relative to the two-site update. In practice, we observe speedups of up to 50% for the Hubbard model, owing to the overheads from the additional operations. The realized acceleration also depends on the specific choice of $\mathscr{D}_p$ and $\mathscr{D}_c$.

IV. BENCHMARKS

In this section, we present benchmarks of the $1s^+$ XTRG algorithm on an analytically solvable free-fermion model. We adopt the following Hamiltonian defined on a one-dimensional open-boundary chain of length L:

$$\mathcal{H} = -t \sum_{i=1}^{L-1} [c_i^\dagger c_{i+1} + c_{i+1}^\dagger c_i]. \tag{18}$$

This Hamiltonian is exactly diagonalizable, yielding eigenvalues $\epsilon_k = -2t\cos(k\pi/(L+1))$ for $k = 1, \ldots, L$. Accordingly, the free energy can be computed as

$$F = -T \sum_{k=1}^{L} \ln(1 + e^{-\beta\epsilon_k}). \tag{19}$$

In our benchmarks, we initialize the density matrix at a high temperature of $\beta = 2^{-12}$ and perform 20 $1s^+$ XTRG iterations to cool the system down to $\beta = 2^8$. Figure 1 displays the relative error of the free energy F as a function of the inverse temperature β, computed via the $1s^+$ XTRG algorithm with bond dimensions $D = 400, 600, 800$, respectively. The numerics indicate that the $1s^+$ XTRG algorithm achieves accuracy comparable to the two-site update scheme [78], while delivering a substantial speedup. Similar plateaulike behaviors are also observed in Ref. [78]. They depend on the bond dimensions and system sizes, and do not carry further physical meaning.

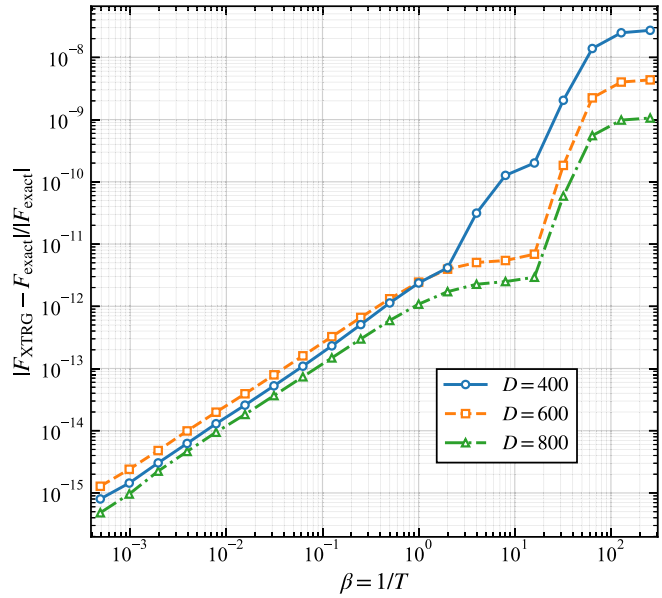

FIG. 1. The error of the free energy F of the free-fermion model of length $L = 64$ relative to the exact value as a function of the inverse temperature β, obtained via the $1s^+$ XTRG algorithm with bond dimension $D = 400, 600, 800$, respectively.

V. ENERGETICS OF THE HUBBARD MODEL

In this section, we juxtapose the energetics of the t-t' Hubbard model obtained from an iPEPS ground-state search with those from XTRG cooling. Our enhanced $1s^+$ XTRG algorithm enables a cooling of the system down to a temperature of $T/t = 1/256$, sufficiently low to warrant a comparison with zero-temperature ground-state studies.

The iPEPS ground-state search is performed on an infinite lattice, achieved by PBC on both x and y directions, with a 4×2 (uniform) or 8×2 (striped) supercell, following [47]. Ground states of distinct characteristics are targeted by constraining the spin symmetry of the tensor network: imposing $\mathrm{SU}(2)_{\mathrm{spin}}$ yields a uniform state, whereas enforcing $\mathrm{U}(1)_{\mathrm{spin}}$ produces a striped state. The uniform states retain $D^* = 7$ multiplets, equivalent to $D = 12$ individual states; for consistency, the striped states are fixed to a bond dimension of $D = 12$.

The XTRG runs start from a high temperature of $\beta = 2^{-12}$ on an 8×8 lattice with PBC along the y direction, and the system is cooled down to $\beta = 2^8$ via 20 $1s^+$ XTRG iterations. Throughout, we preserve $\mathrm{U}(1)_{\mathrm{charge}} \times \mathrm{SU}(2)_{\mathrm{spin}}$ symmetry in the MPO representation of the thermal density matrix, allowing us to retain up to $D^* = 1500$ multiplets (approximately $D \simeq 4000$ individual states). We consider only the $\mathrm{SU}(2)_{\mathrm{spin}}$ symmetry here since continuous symmetry breaking is precluded at finite temperature by the Mermin-Wagner theorem [116,117].

The iPEPS ground states and XTRG density matrices are defined on lattices with differing boundary conditions, which in turn modifies the count of kinetic terms in the

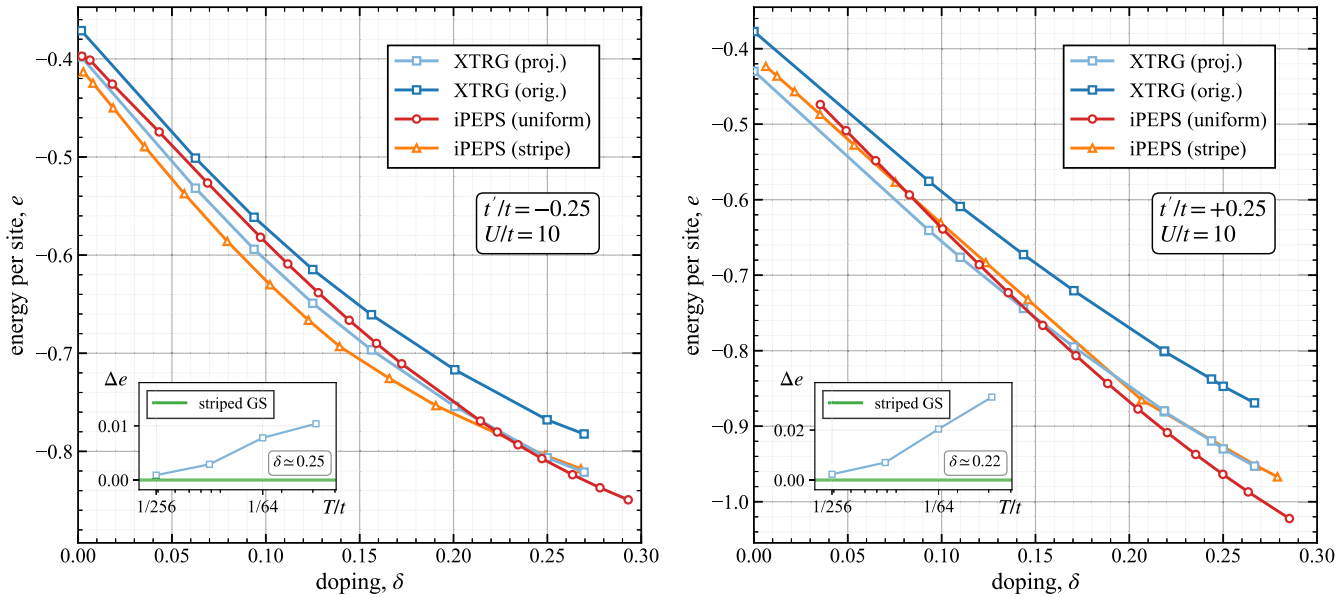

FIG. 2. The ground-state energy per site (red for uniform and orange for striped states) obtained from iPEPS simulations, and the energy at $T/t = 1/256$ (blue) obtained from the $1s^+$ XTRG algorithm. The iPEPS ground states are acquired on an infinite lattice with 4×2 (uniform) or 8×2 (striped) supercell and the XTRG density matrices are generated on an 8×8 lattice with PBC on the y direction. The light blue curves mark the projected energies for the XTRG density matrices with PBC on both directions. The insets show the difference Δe between the projected XTRG energies and the striped iPEPS ground-state (GS) energies with respect to temperature for two representative doping levels.

Hamiltonian. Specifically, an 8×8 lattice with PBC along both x and y directions contains 128 nearest-neighbor (NN) hopping terms and 128 next-nearest-neighbor (NNN) hopping terms, whereas the same lattice with PBC only along the y direction comprises 120 NN terms and 112 NNN terms. To reconcile these discrepancies, we posit bulk-averaged energies for the missing boundary contributions. This leads to a projected (kinetic) energy with

$$\frac{e^{\text{kin}}_{\text{proj}}}{e^{\text{kin}}_{\text{orig}}} = \frac{128e_{\text{NN}} + 128e_{\text{NNN}}}{120e_{\text{NN}} + 112e_{\text{NNN}}}, \tag{20}$$

where e_{NN} and e_{NNN} denote the mean energies of the NN and NNN hopping terms, respectively. This projected energy furnishes a more commensurate reference for comparison with the iPEPS results.

Figure 2 displays the ground-state energy (red for uniform and orange for striped states) obtained from iPEPS simulations, alongside the energy at $T/t = 1/256$ (blue) derived from the $1s^+$ XTRG algorithm. The light blue curves indicate the projected energies for the XTRG density matrices with PBC along both directions.

For both $t'/t = -0.25$ and $t'/t = +0.25$, the projected XTRG energies align well with the iPEPS ground-state energies, showing a similar overall doping dependence. In particular, they lie quite close to the energies of the striped states, which may be attributed to stripe formation induced by the OBC along the x direction in the XTRG simulations. This agreement indicates that our XTRG algorithm attains sufficient purity upon approaching the ultracold regime, i.e., the density matrix $\rho \simeq |\text{GS}\rangle\langle\text{GS}|$ at lowest temperature, where $|\text{GS}\rangle$ is the ground state.

VI. PAIR-PAIR CORRELATIONS

In this section, we investigate the dependence of pairing correlation, which signifies the strength of superconductivity, on doping, temperature, and the sign of t'/t. Rigorously speaking, anomalous local pairing amplitudes are forbidden by the one-dimensionality of the tensor network together with the conserved $\text{U}(1)_{\text{charge}}$ symmetry. We therefore focus on the pair-pair correlations, which quantify the propensity for pair propagation.

Here, we primarily examine the nearest-neighbor singlet pairing correlation

$$\rho_S(\mathbf{r}, \boldsymbol{\alpha}|\mathbf{s}, \boldsymbol{\beta}) = \langle \Delta^\dagger_{\mathbf{r},\mathbf{r}+\boldsymbol{\alpha}} \Delta_{\mathbf{s},\mathbf{s}+\boldsymbol{\beta}} \rangle, \tag{21}$$

where the singlet pairing operator $\Delta_{\mathbf{r},\mathbf{r}+\boldsymbol{\alpha}}$ is defined as

$$\Delta_{\mathbf{r},\mathbf{r}+\boldsymbol{\alpha}} = c_{\mathbf{r},\uparrow} c_{\mathbf{r}+\boldsymbol{\alpha},\downarrow} - c_{\mathbf{r},\downarrow} c_{\mathbf{r}+\boldsymbol{\alpha},\uparrow}, \tag{22}$$

and $\boldsymbol{\alpha} = \mathbf{x}, \mathbf{y}$ denotes the horizontal or vertical unit vector. Following Refs. [60,118], we zero out the contributions whenever $\mathbf{r}$, $\mathbf{r} + \boldsymbol{\alpha}$, $\mathbf{s}$, or $\mathbf{s} + \boldsymbol{\beta}$ are not all distinct. The correlator $\rho_S(\mathbf{r}, \boldsymbol{\alpha}|\mathbf{s}, \boldsymbol{\beta})$, viewed as a matrix with composite indices $(\mathbf{r}, \boldsymbol{\alpha})$ and $(\mathbf{s}, \boldsymbol{\beta})$, can be diagonalized, and one can take the dominant eigenvalue as a scalar indicator of the pairing strength [60,118,119].

Figure 3 presents the dominant eigenvalue of ρ_S as a function of doping δ and temperature T/t, obtained via the $1s^+$ XTRG for $t'/t = -0.25$ (left) and $t'/t = +0.25$ (right). The colored contour map shows the interpolation between discrete data points marked by the red circles.

We observe from Fig. 3 that pairing correlations strengthen with increasing doping δ and decreasing temperature T/t, consistent with the general trends seen in iPEPS ground-state simulations [47] and in cuprate phenomenology. Moreover, the correlations are systematically larger for positive

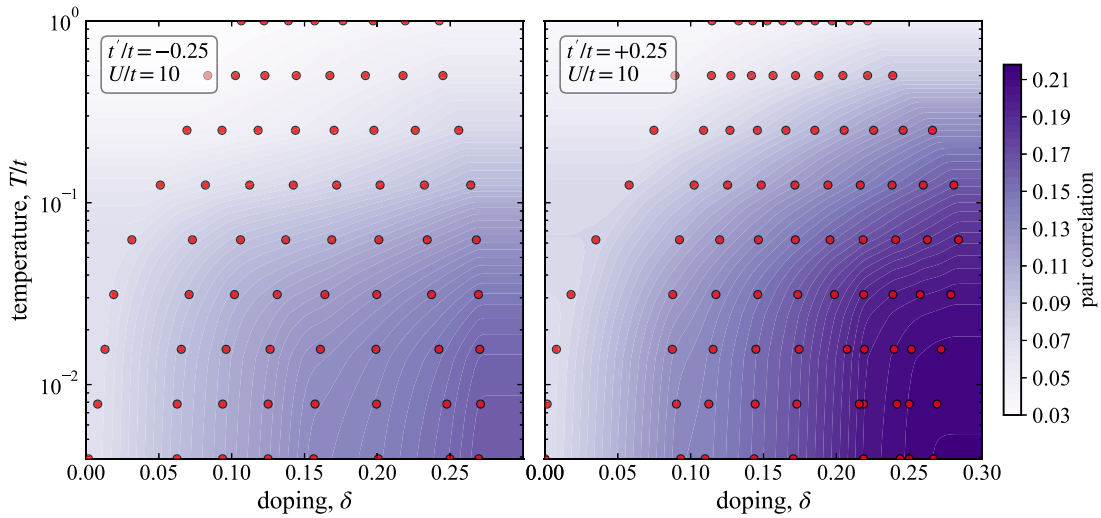

FIG. 3. The pair correlation indicator as a function of doping δ and temperature T/t, obtained from the $1s^+$ XTRG for $t'/t = -0.25$ (left) and $t'/t = +0.25$ (right). Red circles mark the positions with exact data, and the colored contour map displays the interpolation between the data points. The pairing correlation is found strengthened at large doping, low temperature, and a positive t'/t ratio.

t'/t, in line with various ground-state or finite-temperature studies of the t-J [57–59,63–65,89] and Hubbard models [37,44,47,88,111,120]. However, if one adopts the band-structure-based identification that for cuprate superconductors $t'/t > 0$ or < 0 corresponds to electron or hole doping, respectively, our finding that pairing is stronger for $t'/t > 0$ than for $t'/t < 0$ would then be at odds with the experimental observations that pairing is weaker for electron- than hole-doped systems. This emphasizes the need for further investigations of the appropriate parameter settings and effective-model terms relevant for the electron-hole asymmetry of cuprates. Similar tensions have been reported in related t-t'-J and Hubbard studies [58,111,121]. In particular, density- or hole-assisted hopping terms, which can arise when downfolding multiband models to an effective single-band description [42], may be important for capturing the doping-asymmetric carrier mobility and for enhancing pairing on the hole-doped side.

VII. SPIN SUSCEPTIBILITY AND PSEUDOGAP

The pseudogap—manifested as a partial depletion in the electronic density of states—is a hallmark of underdoped cuprate superconductors. Its onset suppresses the low-energy spectral weight and, concomitantly, reduces the uniform spin susceptibility χ_S. In practice, as temperature decreases, χ_S initially follows a Curie-Weiss-like increase, reaches a maximum at a characteristic scale T^*, and subsequently decreases as the pseudogap develops. The locus of this maximum thus provides a practical proxy for the pseudogap onset temperature T^*.

We compute the spin susceptibility by augmenting the Hamiltonian with a Zeeman term, $H_Z = -h\sum_i S_i^z$. The uniform susceptibility is then approximated as

$$\chi_S = -\langle S^z\rangle/h \tag{23}$$

for a sufficiently small external field $h=0.01$, where $S^z = \sum_i S_i^z/L$. To probe the response to a magnetic field, we relax the $SU(2)_{spin}$ symmetry to $U(1)_{spin}$ in these simulations, and retain a maximum bond dimension of $D = 1500$.

Figure 4 compiles χ_S across doping δ and temperature T/t, obtained via the $1s^+$ XTRG for $t'/t = -0.25$ (left) and $t'/t = +0.25$ (right). The colored contour shading interpolates between discrete data points as indicated by red markers. The dashed curve tracks the ridge line of the susceptibility, identifying the onset scale T^* at which the pseudogap begins to emerge.

From the figure, T^* decreases monotonically with increasing δ, with a more pronounced reduction for positive t'/t. These trends are broadly consistent with results for the t-J model [89] and with observations in various cuprate compounds [122–124]. We note that the temperature axis is logarithmic, which visually attenuates the apparent variation of T^* with doping. Besides, the overall magnitude of χ_S is smaller for positive t'/t, indicating a more enhanced pseudogap effect in this regime.

Moreover, for positive t'/t we observe an anomalous low-temperature enhancement of χ_S near $\delta \simeq 0.02$. On an 8×8 lattice, this doping approximately corresponds to a single hole introduced into the half-filled system. The upturn can therefore plausibly be attributed to the formation of a Nagaoka polaron [125–128], which engenders an underlying ferromagnetic tendency and exhibits a strong response to the external magnetic field.

VIII. SAMPLING OF THE DENSITY MATRIX

In this section, we elaborate a straightforward sampling [89] scheme for the thermal density matrix ρ in the format of an MPO. This procedure can be used to generate an ensemble of snapshots (projections onto basis states of the Fock space) for each density matrix at any specified location in phase space. These ensembles can then be assembled into datasets for subsequent artificial intelligence (AI) analyses aimed at uncovering novel, nontrivial features of the Hubbard model.

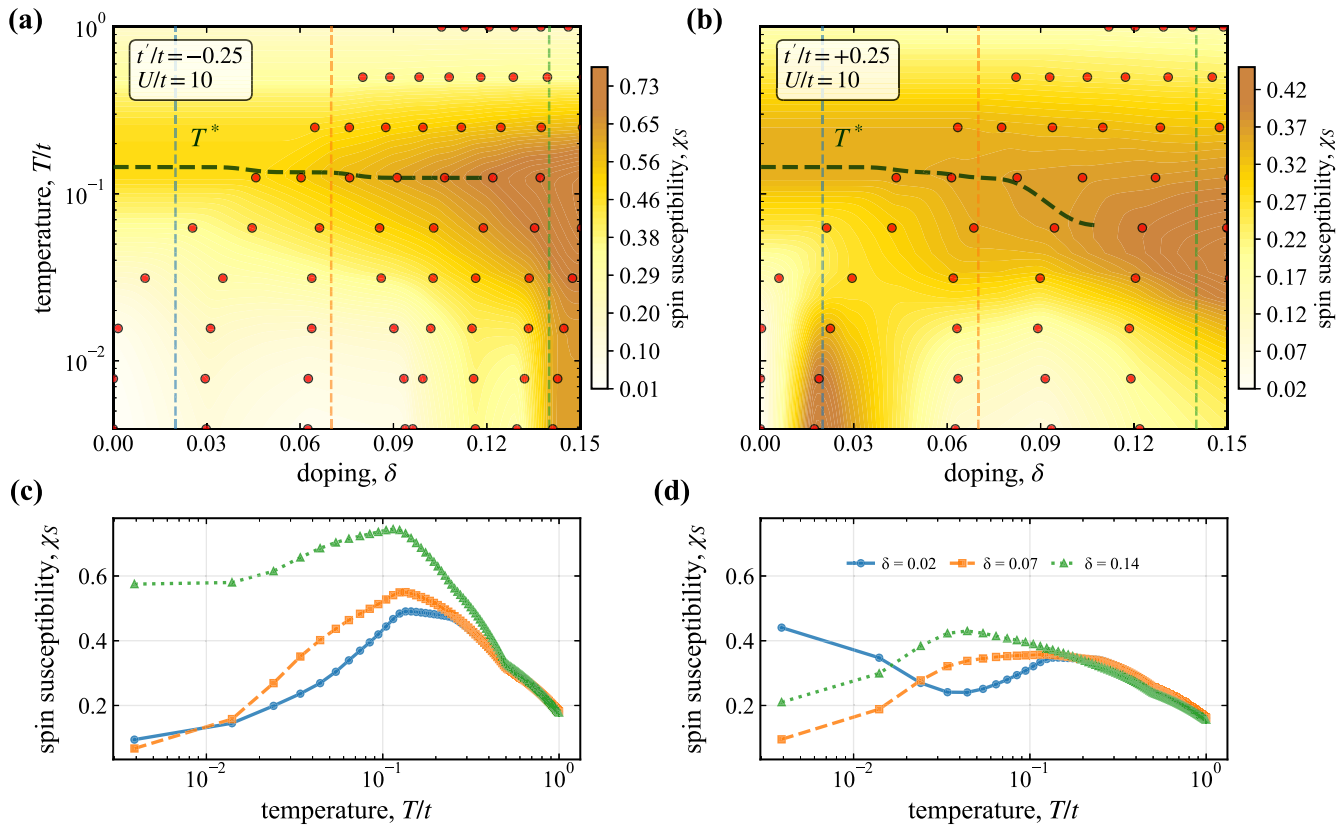

FIG. 4. The spin susceptibility (a), (b) as a function of doping δ and temperature T/t, and (c), (d) as a function of temperature T/t for three representative doping levels (via interpolation), obtained from the $1s^+$ XTRG for (a), (c) $t'/t = -0.25$ and (b), (d) $t'/t = +0.25$. Red circles mark the positions with exact data, and the colored contour map displays the interpolation between the data points. The thick dashed line indicates the locus of the susceptibility peak, signaling the onset temperature T^* where pseudogap starts to develop.

We employ sequential sampling. Specifically, for site i, assuming all sites $\iota < i$ have already been sampled, the single-site reduced density matrix ρ_i can be constructed via the partial trace:

$\rho_i =$ 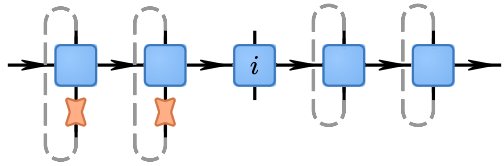 (24)

where the local state projector is defined as

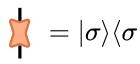 $= |\sigma\rangle\langle\sigma|$ (25)

with σ denoting the sampled local state of the corresponding site. The diagonal entries of ρ_i thus furnish the probability distribution for the local state σ_i at site i. Sampling proceeds by drawing σ_i according to this distribution and then repeating the procedure for the next site $i + 1$.

In this work, we generate snapshot ensembles for the minimal Hubbard model ($t' = 0$) on an 8×8 open-boundary lattice intended for future comparisons with modern ultracold atom experiments [83,97,99,100,103,105,108]. The thermal density matrix MPOs are produced using the $1s^+$ XTRG method across the doping range of $0 < \delta < 0.25$ and down to a lowest temperature of $T/t = 1/256$. To resolve the spin orientation, we relax the symmetry here from $SU(2)_{spin}$ down to $U(1)_{spin}$. Applying the sampling protocol described above, we draw 1000 snapshots for each combination of doping and temperature.

Figure 5 documents the convergence of the hole density n_h and double occupancy n_d as a function of sample size at $\delta \simeq 0.1694$ and $T/t = 1/16$. Green dashed lines indicate reference values extracted directly from the density matrix. We find that satisfactory convergence is achieved for $\gtrsim$200 samples; accordingly, a sample size of 1000 is sufficient to furnish a representative ensemble for the corresponding point in the phase space.

IX. SUMMARY AND OUTLOOK

In this work, we introduced an enhanced $1s^+$ XTRG algorithm that accelerates the cooling of the two-dimensional Hubbard model at finite temperature. By enlarging the accessible variational manifold, the method attains accuracy comparable to a two-site update while incurring computational cost near that of a one-site update, delivering speed-ups of up to 50% for Hubbard-like systems. This improvement enables cooling down to $T/t \approx 0.004$ and supports direct comparisons with zero-temperature iPEPS simulations. We demonstrate that the projected XTRG energies and pairing-correlation characteristics are in close accord with iPEPS ground-state results, indicating that our XTRG

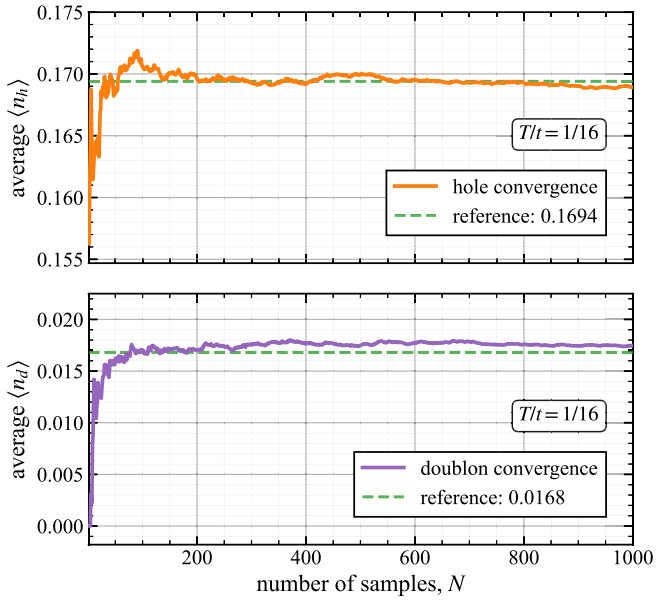

FIG. 5. Convergence behavior of hole density n_h and double occupancy n_d as a function of sample size at $\delta \simeq 0.1694$ and $T/t = 1/16$. Green dashed lines indicate reference values extracted directly from the density matrix.

approach achieves sufficient purity upon entering the ultracold regime.

Our finite-temperature simulations provide a systematic characterization of singlet pairing correlations and spin susceptibilities across a broad range of dopings and temperatures. We find that pairing correlations are enhanced at large doping, low temperature, and for positive t'/t; the latter trend accords with numerous prior numerical studies yet contrasts with behaviors observed in cuprate materials. The pseudogap onset temperature T^* decreases with increasing doping for both signs of t'/t, in line with experimental observations. Finally, we identify an anomalous low-temperature enhancement of the spin susceptibility within a narrow underdoped regime, which may be attributable to the formation of a Nagaoka polaron.

In addition, we leveraged a sequential sampling scheme that generates snapshot ensembles for the minimal Hubbard model, each comprising 1000 samples and shown to be statistically representative of the corresponding point in phase space. These snapshots furnish a data resource for analyzing thermal properties and correlations, opening the door to future AI-driven investigations of the Hubbard model. A comprehensive analysis of this dataset is a topic for future research.

ACKNOWLEDGMENTS

We acknowledge fruitful discussions with Annabelle Bohrdt, Yuan Gao, Ming Huang, Qiaoyi Li, Wei Li, and Dai-Wei Qu. This research was funded in part by the Deutsche Forschungsgemeinschaft under Germany's Excellence Strategy EXC-2111 (Project No. 390814868), and is part of the Munich Quantum Valley, supported by the Bavarian state government through the Hightech Agenda Bayern Plus.

DATA AVAILABILITY

The data that support the findings of this article are not publicly available upon publication because it is not technically feasible and/or the cost of preparing, depositing, and hosting the data would be prohibitive within the terms of this research project. The data are available from the authors upon reasonable request.

[1] J. G. Bednorz and K. A. Müller, Possible high T_c superconductivity in the Ba-La-Cu-O system, Z. Phys. B: Condens. Matter **64**, 189 (1986).
[2] B. Keimer, S. A. Kivelson, M. R. Norman, S. Uchida, and J. Zaanen, From quantum matter to high-temperature superconductivity in copper oxides, Nature (London) **518**, 179 (2015).
[3] C. C. Tsuei and J. R. Kirtley, Pairing symmetry in cuprate superconductors, Rev. Mod. Phys. **72**, 969 (2000).
[4] P. A. Lee, N. Nagaosa, and X.-G. Wen, Doping a Mott insulator: Physics of high-temperature superconductivity, Rev. Mod. Phys. **78**, 17 (2006).
[5] C. Proust and L. Taillefer, The remarkable underlying ground states of cuprate superconductors, Annu. Rev. Condens. Matter Phys. **10**, 409 (2019).
[6] J. Hubbard, Electron correlations in narrow energy bands V. A perturbation expansion about the atomic limit, Proc. R. Soc. Lond. A **296**, 82 (1967).
[7] D. P. Arovas, E. Berg, S. A. Kivelson, and S. Raghu, The Hubbard model, Annu. Rev. Condens. Matter Phys. **13**, 239 (2022).
[8] T. Giamarchi and C. Lhuillier, Phase diagrams of the two-dimensional Hubbard and t-J models by a variational Monte Carlo method, Phys. Rev. B **43**, 12943 (1991).
[9] E. Dagotto, Correlated electrons in high-temperature superconductors, Rev. Mod. Phys. **66**, 763 (1994).
[10] C. J. Halboth and W. Metzner, d-wave superconductivity and Pomeranchuk instability in the two-dimensional Hubbard model, Phys. Rev. Lett. **85**, 5162 (2000).
[11] C. Huscroft, M. Jarrell, Th. Maier, S. Moukouri, and A. N. Tahvildarzadeh, Pseudogaps in the 2D Hubbard model, Phys. Rev. Lett. **86**, 139 (2001).
[12] S. R. White and D. J. Scalapino, Stripes on a 6-leg Hubbard ladder, Phys. Rev. Lett. **91**, 136403 (2003).
[13] G. Hager, G. Wellein, E. Jeckelmann, and H. Fehske, Stripe formation in doped Hubbard ladders, Phys. Rev. B **71**, 075108 (2005).
[14] A. Macridin, M. Jarrell, T. Maier, P. R. C. Kent, and E. D'Azevedo, Pseudogap and antiferromagnetic correlations in the Hubbard model, Phys. Rev. Lett. **97**, 036401 (2006).
[15] T. A. Maier, M. Jarrell, T. C. Schulthess, P. R. C. Kent, and J. B. White, Systematic study of d -wave superconductivity in the 2D repulsive Hubbard model, Phys. Rev. Lett. **95**, 237001 (2005).
[16] M. Capone and G. Kotliar, Competition between d-wave superconductivity and antiferromagnetism in the two-dimensional Hubbard model, Phys. Rev. B **74**, 054513 (2006).

[17] D. J. Scalapino, The 2D Hubbard model and the high T_c cuprate problem, J. Supercond. Novel Magn. **19**, 195 (2007).
[18] C.-C. Chang and S. Zhang, Spin and charge order in the doped Hubbard model: Long-wavelength collective modes, Phys. Rev. Lett. **104**, 116402 (2010).
[19] G. Sordi, P. Sémon, K. Haule, and A.-M. S. Tremblay, Strong coupling superconductivity, pseudogap, and Mott transition, Phys. Rev. Lett. **108**, 216401 (2012).
[20] H. Yokoyama, M. Ogata, Y. Tanaka, K. Kobayashi, and H. Tsuchiura, Crossover between BCS superconductor and doped Mott insulator of d-wave pairing state in two-dimensional Hubbard model, J. Phys. Soc. Jpn. **82**, 014707 (2013).
[21] E. Gull, O. Parcollet, and A. J. Millis, Superconductivity and the pseudogap in the two-dimensional Hubbard model, Phys. Rev. Lett. **110**, 216405 (2013).
[22] J. Otsuki, H. Hafermann, and A. I. Lichtenstein, Superconductivity, antiferromagnetism, and phase separation in the two-dimensional Hubbard model: A dual-fermion approach, Phys. Rev. B **90**, 235132 (2014).
[23] J. P. F. LeBlanc, A. E. Antipov, F. Becca, I. W. Bulik, G. K.-L. Chan, C.-M. Chung, Y. Deng, M. Ferrero, T. M. Henderson, C. A. Jiménez-Hoyos, E. Kozik, X.-W. Liu, A. J. Millis, N. V. Prokof'ev, M. Qin, G. E. Scuseria, H. Shi, B. V. Svistunov, L. F. Tocchio, I. S. Tupitsyn, *et al.*, Solutions of the two-dimensional Hubbard model: Benchmarks and results from a wide range of numerical algorithms, Phys. Rev. X **5**, 041041 (2015).
[24] Y. Deng, E. Kozik, N. V. Prokof'ev, and B. V. Svistunov, Emergent BCS regime of the two-dimensional fermionic Hubbard model: Ground-state phase diagram, Europhys. Lett. **110**, 57001 (2015).
[25] P. Corboz, Improved energy extrapolation with infinite projected entangled-pair states applied to the two-dimensional Hubbard model, Phys. Rev. B **93**, 045116 (2016).
[26] L. F. Tocchio, F. Becca, and S. Sorella, Hidden Mott transition and large-U superconductivity in the two-dimensional Hubbard model, Phys. Rev. B **94**, 195126 (2016).
[27] B.-X. Zheng and G. K.-L. Chan, Ground-state phase diagram of the square lattice Hubbard model from density matrix embedding theory, Phys. Rev. B **93**, 035126 (2016).
[28] B.-X. Zheng, C.-M. Chung, P. Corboz, G. Ehlers, M.-P. Qin, R. M. Noack, H. Shi, S. R. White, S. Zhang, and G. K.-L. Chan, Stripe order in the underdoped region of the two-dimensional Hubbard model, Science **358**, 1155 (2017).
[29] H.-H. Zhao, K. Ido, S. Morita, and M. Imada, Variational Monte Carlo method for fermionic models combined with tensor networks and applications to the hole-doped two-dimensional Hubbard model, Phys. Rev. B **96**, 085103 (2017).
[30] A. S. Darmawan, Y. Nomura, Y. Yamaji, and M. Imada, Stripe and superconducting order competing in the Hubbard model on a square lattice studied by a combined variational Monte Carlo and tensor network method, Phys. Rev. B **98**, 205132 (2018).
[31] T. I. Vanhala and P. Törmä, Dynamical mean-field theory study of stripe order and d-wave superconductivity in the two-dimensional Hubbard model, Phys. Rev. B **97**, 075112 (2018).
[32] B. Ponsioen, S. S. Chung, and P. Corboz, Period 4 stripe in the extended two-dimensional Hubbard model, Phys. Rev. B **100**, 195141 (2019).
[33] H.-C. Jiang and T. P. Devereaux, Superconductivity in the doped Hubbard model and its interplay with next-nearest hopping t′, Science **365**, 1424 (2019).
[34] N. J. Robinson, P. D. Johnson, T. M. Rice, and A. M. Tsvelik, Anomalies in the pseudogap phase of the cuprates: Competing ground states and the role of umklapp scattering, Rep. Prog. Phys. **82**, 126501 (2019).
[35] Y.-F. Jiang, J. Zaanen, T. P. Devereaux, and H.-C. Jiang, Ground state phase diagram of the doped Hubbard model on the four-leg cylinder, Phys. Rev. Res. **2**, 033073 (2020).
[36] M. Qin, C.-M. Chung, H. Shi, E. Vitali, C. Hubig, U. Schollwöck, S. R. White, S. Zhang, *et al.* (Simons Collaboration on the Many-Electron Problem), Absence of superconductivity in the pure two-dimensional Hubbard model, Phys. Rev. X **10**, 031016 (2020).
[37] C.-M. Chung, M. Qin, S. Zhang, U. Schollwöck, and S. R. White, Plaquette versus ordinary d -wave pairing in the t' -Hubbard model on a width-4 cylinder, Phys. Rev. B **102**, 041106(R) (2020).
[38] X. Dong, L. Del Re, A. Toschi, and E. Gull, Mechanism of superconductivity in the Hubbard model at intermediate interaction strength, Proc. Natl. Acad. Sci. USA **119**, e2205048119 (2022).
[39] X. Dong, E. Gull, and A. J. Millis, Quantifying the role of antiferromagnetic fluctuations in the superconductivity of the doped Hubbard model, Nature Phys. **18**, 1293 (2022).
[40] M. Qin, T. Schäfer, S. Andergassen, P. Corboz, and E. Gull, The Hubbard model: A computational perspective, Annu. Rev. Condens. Matter Phys. **13**, 275 (2022).
[41] H. Xu, H. Shi, E. Vitali, M. Qin, and S. Zhang, Stripes and spin-density waves in the doped two-dimensional Hubbard model: Ground state phase diagram, Phys. Rev. Res. **4**, 013239 (2022).
[42] S. Jiang, D. J. Scalapino, and S. R. White, Density matrix renormalization group based downfolding of the three-band Hubbard model: Importance of density-assisted hopping, Phys. Rev. B **108**, L161111 (2023).
[43] B. Xiao, Y.-Y. He, A. Georges, and S. Zhang, Temperature dependence of spin and charge orders in the doped two-dimensional Hubbard model, Phys. Rev. X **13**, 011007 (2023).
[44] Y.-F. Jiang, T. P. Devereaux, and H.-C. Jiang, Ground-state phase diagram and superconductivity of the doped Hubbard model on six-leg square cylinders, Phys. Rev. B **109**, 085121 (2024).
[45] H. Xu, C.-M. Chung, M. Qin, U. Schollwöck, S. R. White, and S. Zhang, Coexistence of superconductivity with partially filled stripes in the Hubbard model, Science **384**, eadh7691 (2024).
[46] S. d. A. Sousa-Júnior, N. C. Costa, and R. R. dos Santos, Half-filled extended Hubbard model on a square lattice: Phase boundaries from determinant quantum Monte Carlo simulations, Phys. Rev. B **109**, 165102 (2024).
[47] C. Zhang, J.-W. Li, D. Nikolaidou, and J. von Delft, Frustration-induced superconductivity in the $t - t'$ Hubbard model, Phys. Rev. Lett. **134**, 116502 (2025).
[48] S. R. White and D. J. Scalapino, Density matrix renormalization group study of the striped phase in the 2D $t - J$ model, Phys. Rev. Lett. **80**, 1272 (1998).

[49] W.-J. Hu, F. Becca, and S. Sorella, Absence of static stripes in the two-dimensional $t-J$ model determined using an accurate and systematic quantum Monte Carlo approach, Phys. Rev. B **85**, 081110(R) (2012).

[50] P. Corboz, T. M. Rice, and M. Troyer, Competing states in the $t-J$ model: Uniform d-wave state versus stripe state, Phys. Rev. Lett. **113**, 046402 (2014).

[51] J. F. Dodaro, H.-C. Jiang, and S. A. Kivelson, Intertwined order in a frustrated four-leg $t-J$ cylinder, Phys. Rev. B **95**, 155116 (2017).

[52] H.-C. Jiang, Z.-Y. Weng, and S. A. Kivelson, Superconductivity in the doped $t-J$ model: Results for four-leg cylinders, Phys. Rev. B **98**, 140505(R) (2018).

[53] C. Hubig, A. Bohrdt, M. Knap, F. Grusdt, and I. Cirac, Evaluation of time-dependent correlators after a local quench in iPEPS: Hole motion in the t-J model, SciPost Phys. **8**, 021 (2020).

[54] H.-C. Jiang, S. Chen, and Z.-Y. Weng, Critical role of the sign structure in the doped Mott insulator: Luther-Emery versus Fermi-liquid-like state in quasi-one-dimensional ladders, Phys. Rev. B **102**, 104512 (2020).

[55] H.-C. Jiang and S. A. Kivelson, High temperature superconductivity in a lightly doped quantum spin liquid, Phys. Rev. Lett. **127**, 097002 (2021).

[56] J.-W. Li, B. Bruognolo, A. Weichselbaum, and J. von Delft, Study of spin symmetry in the doped $t-J$ model using infinite projected entangled pair states, Phys. Rev. B **103**, 075127 (2021).

[57] S. Gong, W. Zhu, and D. N. Sheng, Robust d-wave superconductivity in the square-lattice $t-J$ model, Phys. Rev. Lett. **127**, 097003 (2021).

[58] S. Jiang, D. J. Scalapino, and S. R. White, Ground-state phase diagram of the t-t'-J model, Proc. Natl. Acad. Sci. USA **118**, e2109978118 (2021).

[59] S. Jiang, D. J. Scalapino, and S. R. White, Pairing properties of the $t-t'-t''-J$ model, Phys. Rev. B **106**, 174507 (2022).

[60] A. Wietek, Fragmented Cooper pair condensation in striped superconductors, Phys. Rev. Lett. **129**, 177001 (2022).

[61] H.-C. Jiang, S. A. Kivelson, and D.-H. Lee, Superconducting valence bond fluid in lightly doped eight-leg $t-J$ cylinders, Phys. Rev. B **108**, 054505 (2023).

[62] X. Lu, D.-W. Qu, Y. Qi, W. Li, and S.-S. Gong, Ground-state phase diagram of the extended two-leg $t-J$ ladder, Phys. Rev. B **107**, 125114 (2023).

[63] X. Lu, F. Chen, W. Zhu, D. N. Sheng, and S.-S. Gong, Emergent superconductivity and competing charge orders in hole-doped square-lattice $t-J$ model, Phys. Rev. Lett. **132**, 066002 (2024).

[64] X. Lu, J.-X. Zhang, S.-S. Gong, D. N. Sheng, and Z.-Y. Weng, Sign structure of the $t-t'-J$ model and its physical consequences, Phys. Rev. B **110**, 165127 (2024).

[65] X. Lu, H. Guo, W.-Q. Chen, D. N. Sheng, and S.-S. Gong, Tuning competition between charge order and superconductivity in the square-lattice $t-t'-J$ model, Phys. Rev. B **111**, 035139 (2025).

[66] J. Jaklič and P. Prelovšek, Lanczos method for the calculation of finite-temperature quantities in correlated systems, Phys. Rev. B **49**, 5065 (1994).

[67] J. Jaklič and P. Prelovšek, Thermodynamic properties of the planar $t-J$ model, Phys. Rev. Lett. **77**, 892 (1996).

[68] J. Jaklič and P. Prelovšek, Finite-temperature properties of doped antiferromagnets, Adv. Phys. **49**, 1 (2000).

[69] K.-S. Chen, Z. Y. Meng, S.-X. Yang, T. Pruschke, J. Moreno, and M. Jarrell, Evolution of the superconductivity dome in the two-dimensional Hubbard model, Phys. Rev. B **88**, 245110 (2013).

[70] Y.-Y. He, M. Qin, H. Shi, Z.-Y. Lu, and S. Zhang, Finite-temperature auxiliary-field quantum Monte Carlo: Self-consistent constraint and systematic approach to low temperatures, Phys. Rev. B **99**, 045108 (2019).

[71] S. R. White, Minimally entangled typical quantum states at finite temperature, Phys. Rev. Lett. **102**, 190601 (2009).

[72] E. M. Stoudenmire and S. R. White, Minimally entangled typical thermal state algorithms, New J. Phys. **12**, 055026 (2010).

[73] W. Li, S.-J. Ran, S.-S. Gong, Y. Zhao, B. Xi, F. Ye, and G. Su, Linearized tensor renormalization group algorithm for the calculation of thermodynamic properties of quantum lattice models, Phys. Rev. Lett. **106**, 127202 (2011).

[74] P. Czarnik, L. Cincio, and J. Dziarmaga, Projected entangled pair states at finite temperature: Imaginary time evolution with ancillas, Phys. Rev. B **86**, 245101 (2012).

[75] P. Czarnik and J. Dziarmaga, Fermionic projected entangled pair states at finite temperature, Phys. Rev. B **90**, 035144 (2014).

[76] P. Czarnik and J. Dziarmaga, Variational approach to projected entangled pair states at finite temperature, Phys. Rev. B **92**, 035152 (2015).

[77] P. Czarnik, M. M. Rams, and J. Dziarmaga, Variational tensor network renormalization in imaginary time: Benchmark results in the Hubbard model at finite temperature, Phys. Rev. B **94**, 235142 (2016).

[78] B.-B. Chen, L. Chen, Z. Chen, W. Li, and A. Weichselbaum, Exponential thermal tensor network approach for quantum lattice models, Phys. Rev. X **8**, 031082 (2018).

[79] L. Chen, D.-W. Qu, H. Li, B.-B. Chen, S.-S. Gong, J. von Delft, A. Weichselbaum, and W. Li, Two-temperature scales in the triangular-lattice Heisenberg antiferromagnet, Phys. Rev. B **99**, 140404(R) (2019).

[80] P. Czarnik, J. Dziarmaga, and P. Corboz, Time evolution of an infinite projected entangled pair state: An efficient algorithm, Phys. Rev. B **99**, 035115 (2019).

[81] P. Czarnik and P. Corboz, Finite correlation length scaling with infinite projected entangled pair states at finite temperature, Phys. Rev. B **99**, 245107 (2019).

[82] H. Li, B.-B. Chen, Z. Chen, J. von Delft, A. Weichselbaum, and W. Li, Thermal tensor renormalization group simulations of square-lattice quantum spin models, Phys. Rev. B **100**, 045110 (2019).

[83] B.-B. Chen, C. Chen, Z. Chen, J. Cui, Y. Zhai, A. Weichselbaum, J. von Delft, Z. Y. Meng, and W. Li, Quantum many-body simulations of the two-dimensional Fermi-Hubbard model in ultracold optical lattices, Phys. Rev. B **103**, L041107 (2021).

[84] A. Wietek, R. Rossi, F. Šimkovic, M. Klett, P. Hansmann, M. Ferrero, E. M. Stoudenmire, T. Schäfer, and A. Georges, Mott insulating states with competing orders in the triangular lattice Hubbard model, Phys. Rev. X **11**, 041013 (2021).

[85] A. Wietek, Y.-Y. He, S. R. White, A. Georges, and E. M. Stoudenmire, Stripes, antiferromagnetism, and the pseudogap

in the doped Hubbard model at finite temperature, Phys. Rev. X **11**, 031007 (2021).

[86] X. Lin, B.-B. Chen, W. Li, Z. Y. Meng, and T. Shi, Exciton proliferation and fate of the topological Mott insulator in a twisted bilayer graphene lattice model, Phys. Rev. Lett. **128**, 157201 (2022).

[87] A. Sinha, M. M. Rams, P. Czarnik, and J. Dziarmaga, Finite-temperature tensor network study of the Hubbard model on an infinite square lattice, Phys. Rev. B **106**, 195105 (2022).

[88] Q. Li, Y. Gao, Y.-Y. He, Y. Qi, B.-B. Chen, and W. Li, Tangent space approach for thermal tensor network simulations of the 2D Hubbard model, Phys. Rev. Lett. **130**, 226502 (2023).

[89] D.-W. Qu, Q. Li, S.-S. Gong, Y. Qi, W. Li, and G. Su, Phase diagram, d -wave superconductivity, and pseudogap of the $t-t'-J$ model at finite temperature, Phys. Rev. Lett. **133**, 256003 (2024).

[90] A. Gleis, J.-W. Li, and J. von Delft, Projector formalism for kept and discarded spaces of matrix product states, Phys. Rev. B **106**, 195138 (2022).

[91] A. Gleis, J.-W. Li, and J. von Delft, Controlled bond expansion for density matrix renormalization group ground state search at single-site costs, Phys. Rev. Lett. **130**, 246402 (2023).

[92] J.-W. Li, A. Gleis, and J. von Delft, Time-dependent variational principle with controlled bond expansion for matrix product states, Phys. Rev. Lett. **133**, 026401 (2024).

[93] A. Bohrdt, C. S. Chiu, G. Ji, M. Xu, D. Greif, M. Greiner, E. Demler, F. Grusdt, and M. Knap, Classifying snapshots of the doped Hubbard model with machine learning, Nature Phys. **15**, 921 (2019).

[94] C. S. Chiu, G. Ji, A. Bohrdt, M. Xu, M. Knap, E. Demler, F. Grusdt, M. Greiner, and D. Greif, String patterns in the doped Hubbard model, Science **365**, 251 (2019).

[95] A. Mazurenko, C. S. Chiu, G. Ji, M. F. Parsons, M. Kanász-Nagy, R. Schmidt, F. Grusdt, E. Demler, D. Greif, and M. Greiner, A cold-atom Fermi–Hubbard antiferromagnet, Nature (London) **545**, 462 (2017).

[96] C. S. Chiu, G. Ji, A. Mazurenko, D. Greif, and M. Greiner, Quantum state engineering of a Hubbard system with ultracold fermions, Phys. Rev. Lett. **120**, 243201 (2018).

[97] J. Koepsell, J. Vijayan, P. Sompet, F. Grusdt, T. A. Hilker, E. Demler, G. Salomon, I. Bloch, and C. Gross, Imaging magnetic polarons in the doped Fermi–Hubbard model, Nature (London) **572**, 358 (2019).

[98] G. Salomon, J. Koepsell, J. Vijayan, T. A. Hilker, J. Nespolo, L. Pollet, I. Bloch, and C. Gross, Direct observation of incommensurate magnetism in Hubbard chains, Nature (London) **565**, 56 (2019).

[99] J. Koepsell, S. Hirthe, D. Bourgund, P. Sompet, J. Vijayan, G. Salomon, C. Gross, and I. Bloch, Robust bilayer charge pumping for spin- and density-resolved quantum gas microscopy, Phys. Rev. Lett. **125**, 010403 (2020).

[100] J. Koepsell, D. Bourgund, P. Sompet, S. Hirthe, A. Bohrdt, Y. Wang, F. Grusdt, E. Demler, G. Salomon, C. Gross, and I. Bloch, Microscopic evolution of doped Mott insulators from polaronic metal to Fermi liquid, Science **374**, 82 (2021).

[101] P. Sompet, S. Hirthe, D. Bourgund, T. Chalopin, J. Bibo, J. Koepsell, P. Bojović, R. Verresen, F. Pollmann, G. Salomon, C. Gross, T. A. Hilker, and I. Bloch, Realizing the symmetry-protected Haldane phase in Fermi–Hubbard ladders, Nature (London) **606**, 484 (2022).

[102] S. Hirthe, T. Chalopin, D. Bourgund, P. Bojović, A. Bohrdt, E. Demler, F. Grusdt, I. Bloch, and T. A. Hilker, Magnetically mediated hole pairing in fermionic ladders of ultracold atoms, Nature (London) **613**, 463 (2023).

[103] M. Xu, L. H. Kendrick, A. Kale, Y. Gang, G. Ji, R. T. Scalettar, M. Lebrat, and M. Greiner, Frustration- and doping-induced magnetism in a Fermi–Hubbard simulator, Nature (London) **620**, 971 (2023).

[104] T. Chalopin, P. Bojović, S. Wang, T. Franz, A. Sinha, Z. Wang, D. Bourgund, J. Obermeyer, F. Grusdt, A. Bohrdt, L. Pollet, A. Wietek, A. Georges, T. Hilker, and I. Bloch, Observation of emergent scaling of spin-charge correlations at the onset of the pseudogap, Proc. Natl. Acad. Sci. USA **123**, e2525539123 (2026).

[105] G. Pasqualetti, O. Bettermann, N. Darkwah Oppong, E. Ibarra-García-Padilla, S. Dasgupta, R. T. Scalettar, K. R. A. Hazzard, I. Bloch, and S. Fölling, Equation of state and thermometry of the 2D $SU(N)$ Fermi-Hubbard model, Phys. Rev. Lett. **132**, 083401 (2024).

[106] D. Bourgund, T. Chalopin, P. Bojović, H. Schlömer, S. Wang, T. Franz, S. Hirthe, A. Bohrdt, F. Grusdt, I. Bloch, and T. A. Hilker, Formation of individual stripes in a mixed-dimensional cold-atom Fermi–Hubbard system, Nature (London) **637**, 57 (2025).

[107] T. Chalopin, P. Bojović, D. Bourgund, S. Wang, T. Franz, I. Bloch, and T. Hilker, Optical superlattice for engineering Hubbard couplings in quantum simulation, Phys. Rev. Lett. **134**, 053402 (2025).

[108] M. Xu, L. H. Kendrick, A. Kale, Y. Gang, C. Feng, S. Zhang, A. W. Young, M. Lebrat, and M. Greiner, A neutral-atom Hubbard quantum simulator in the cryogenic regime, Nature (London) **642**, 909 (2025).

[109] M. Hirayama, Y. Yamaji, T. Misawa, and M. Imada, *Ab initio* effective Hamiltonians for cuprate superconductors, Phys. Rev. B **98**, 134501 (2018).

[110] M. Hirayama, T. Misawa, T. Ohgoe, Y. Yamaji, and M. Imada, Effective Hamiltonian for cuprate superconductors derived from multiscale *ab initio* scheme with level renormalization, Phys. Rev. B **99**, 245155 (2019).

[111] W. O. Wang and T. P. Devereaux, Finite-temperature signatures of underlying superconductivity in the electron-doped Hubbard model, arXiv:2510.16616 [cond-mat].

[112] A. Weichselbaum, Non-Abelian symmetries in tensor networks: A quantum symmetry space approach, Ann. Phys. (N.Y.) **327**, 2972 (2012).

[113] A. Weichselbaum, X-symbols for non-Abelian symmetries in tensor networks, Phys. Rev. Res. **2**, 023385 (2020).

[114] A. Weichselbaum, QSpace - An open-source tensor library for Abelian and non-Abelian symmetries, SciPost Phys. Codebases 40 (2024).

[115] A. Weichselbaum, Open source QSpace tensor library v4.0, https://bitbucket.org/qspace4u.

[116] N. D. Mermin and H. Wagner, Absence of ferromagnetism or antiferromagnetism in one- or two-dimensional isotropic Heisenberg models, Phys. Rev. Lett. **17**, 1307 (1966).

[117] P. C. Hohenberg, Existence of long-range order in one and two dimensions, Phys. Rev. **158**, 383 (1967).

[118] N. Baldelli, H. Karlsson, B. Kloss, M. Fishman, and A. Wietek, Fragmented superconductivity in the Hubbard model as

solitons in Ginzburg–Landau theory, npj Quantum Mater. **10**, 22 (2025).

[119] O. Penrose and L. Onsager, Bose-Einstein condensation and liquid helium, Phys. Rev. **104**, 576 (1956).

[120] F. Chen, F. D. M. Haldane, and D. N. Sheng, Global phase diagram of d-wave superconductivity in the square-lattice *t*-*J* model, Proc. Natl. Acad. Sci. USA **122**, e2420963122 (2025).

[121] T. Xiang, H. G. Luo, D. H. Lu, K. M. Shen, and Z. X. Shen, Intrinsic electron and hole bands in electron-doped cuprate superconductors, Phys. Rev. B **79**, 014524 (2009).

[122] B. Loret, S. Sakai, S. Benhabib, Y. Gallais, M. Cazayous, M. A. Méasson, R. D. Zhong, J. Schneeloch, G. D. Gu, A. Forget, D. Colson, I. Paul, M. Civelli, and A. Sacuto, Vertical temperature boundary of the pseudogap under the superconducting dome in the phase diagram of $Bi_2Sr_2CaCu_2O_8 + \delta$, Phys. Rev. B **96**, 094525 (2017).

[123] F. Boschini, M. Zonno, E. Razzoli, R. P. Day, M. Michiardi, B. Zwartsenberg, P. Nigge, M. Schneider, E. H. da Silva Neto, A. Erb, S. Zhdanovich, A. K. Mills, G. Levy, C. Giannetti, D. J. Jones, and A. Damascelli, Emergence of pseudogap from short-range spin-correlations in electron-doped cuprates, npj Quantum Mater. **5**, 6 (2020).

[124] G. Grissonnanche, O. Cyr-Choinière, J. Day, R. Liang, D. A. Bonn, W. N. Hardy, N. Doiron-Leyraud, and L. Taillefer, No nematicity at the onset temperature of the pseudogap phase in the cuprate superconductor $YBa_2Cu_3O_y$, Phys. Rev. X **13**, 031010 (2023).

[125] Y. Nagaoka, Ferromagnetism in a narrow, almost half-filled *s* band, Phys. Rev. **147**, 392 (1966).

[126] H. Tasaki, From Nagaoka's ferromagnetism to flat-band ferromagnetism and beyond: An introduction to ferromagnetism in the Hubbard model, Prog. Theor. Phys. **99**, 489 (1998).

[127] M. Lebrat, M. Xu, L. H. Kendrick, A. Kale, Y. Gang, P. Seetharaman, I. Morera, E. Khatami, E. Demler, and M. Greiner, Observation of Nagaoka polarons in a Fermi–Hubbard quantum simulator, Nature (London) **629**, 317 (2024).

[128] R. Samajdar and R. N. Bhatt, Polaronic mechanism of Nagaoka ferromagnetism in Hubbard models, Phys. Rev. B **109**, 235128 (2024).